
PICS IN PICS: PHYSICS INFORMED CONTOUR SELECTION FOR RAPID IMAGE SEGMENTATION

Vikas Dwivedi

Atmospheric Science Research Center
State University of New York, Albany
New York, 12222, USA
vdwivedi@albany.edu

Balaji Srinivasan

Department of Mechanical Engineering
Indian Institute of Technology, Madras
Chennai, 600036, India
sbalaji@iitm.ac.in

Ganapathy Krishnamurthi

Department of Engineering Design
Indian Institute of Technology, Madras
Chennai, 600036, India
gankrish@iitm.ac.in

ABSTRACT

Effective training of deep image segmentation models is challenging due to the need for abundant, high-quality annotations. Generating annotations is laborious and time-consuming for human experts, especially in medical image segmentation. To facilitate image annotation, we introduce Physics Informed Contour Selection (PICS) - an interpretable, physics-informed algorithm for rapid image segmentation without relying on labeled data. PICS draws inspiration from physics-informed neural networks (PINNs) and an active contour model called snake. It is fast and computationally lightweight because it employs cubic splines instead of a deep neural network as a basis function. Its training parameters are physically interpretable because they directly represent control knots of the segmentation curve. Traditional snakes involve minimization of the edge-based loss functionals by deriving the Euler-Lagrange equation followed by its numerical solution. However, PICS directly minimizes the loss functional, bypassing the Euler Lagrange equations. It is the first snake variant to minimize a region-based loss function instead of traditional edge-based loss functions. PICS uniquely models the three-dimensional (3D) segmentation process with an unsteady partial differential equation (PDE), which allows accelerated segmentation via transfer learning. To demonstrate its effectiveness, we apply PICS for 3D segmentation of the left ventricle on a publicly available cardiac dataset. While doing so, we also introduce a new convexity-preserving loss term that encodes the shape information of the left ventricle to enhance PICS's segmentation quality. Overall, PICS presents several novelties in network architecture, transfer learning, and physics-inspired losses for image segmentation, thereby showing promising outcomes and potential for further refinement.

Keywords Physics Informed Neural Network · Active Contour Model · Image Segmentation · Chan-Vese Functional · Transfer Learning

1 Introduction

Deep learning-based computer vision models have achieved remarkable success in various medical imaging tasks. However, their reliance on large amounts of labeled data can limit their utility in situations where data is scarce or unavailable. This limitation has spurred significant recent advancements in the field of physics-informed computer vision (PICV), as discussed in Banerjee et al. [1].

The term "physics-informed" in PICV is largely attributed to the development of the Physics Informed Neural Network (PINN) by Raissi et al. [2]. PINNs have shown promise in addressing forward and inverse problems related to partial

differential equations (PDEs) in fields like fluid mechanics [3, 4], material modeling [5], heat transfer [6, 7], and more [8].

Inspired by the philosophy behind PINNs, PICV integrates physical principles into machine learning frameworks for computer vision. This approach results in faster, more interpretable, and data-efficient computer vision models. In context of medical imaging, some recent examples are as follows. Lopez et al.[9] recently introduced WarpPINN, a physics-informed neural network designed for image registration to assess local metrics of heart deformation. They incorporated the near-incompressibility of cardiac tissue by penalizing the Jacobian of the deformation field. Similarly, Vries et al.[10] developed a PINN-based model to estimate CT perfusion parameters from noisy data related to acute ischemic stroke. Herten et al.[11] utilized PINNs for tracer-kinetic modeling and parameter inference using myocardial perfusion medical resonance imaging (MRI) data. Buoso and collaborators proposed a parametric PINN for simulating personalized left-ventricular biomechanics, offering the potential to significantly expedite training data synthesis [12]. Additionally, Burwinkel et al.[13] introduced OpticNet, an innovative optical refraction network that utilizes an unsupervised, domain-specific loss function to explicitly incorporate ophthalmological information into the network.

Our primary focus in this study is image segmentation, which involves identifying and delineating distinct regions or objects within an image. The approaches to image segmentation can be broadly categorized into two extremes: deep learning-based models that rely on substantial labeled training data and traditional models that do not require training data but face challenges related to some theoretical and numerical aspects.

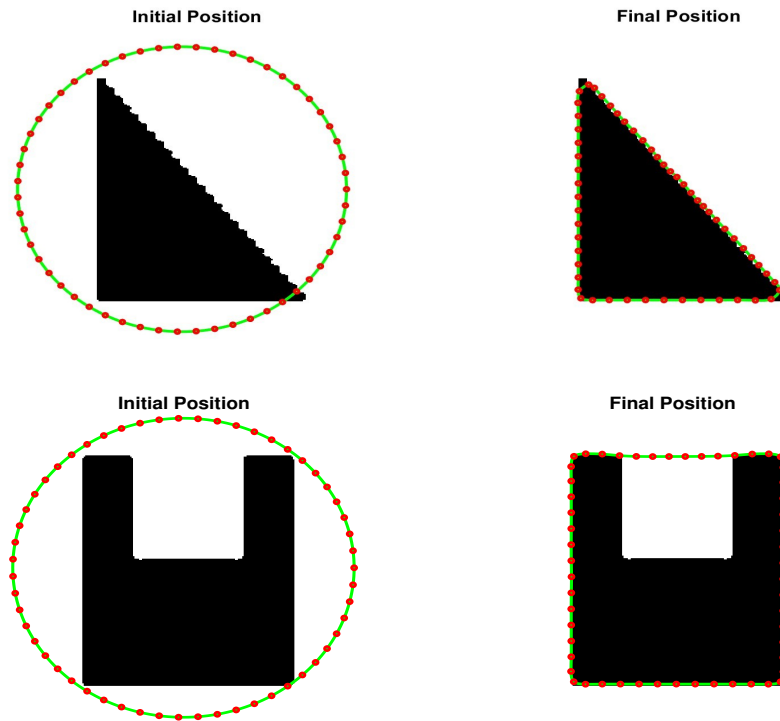


Figure 1: Image segmentation with a naive image gradient-based snake. In the cavity case, please note that it gets stuck to a local minima.

Among all active contour models, snake[14] is the most intuitive image segmentation model. It is based on the concept of a deformable curve or surface that can be iteratively adjusted to fit the edges or boundaries of an object in an image. The contour is driven by internal energy, which represents the smoothness of the curve, and external energy, which is derived from image features such as intensity or texture. By minimizing the total energy, the contour can accurately delineate the object boundaries, thus facilitating object recognition and tracking. For example, refer to Fig.1. At the start, the snake (or deformable contour) has maximum energy, and following the minimization process, it converges

to the object’s boundary. In mathematical terms, snakes detect object boundaries by minimizing edge-based energy functionals, achieved through the solution of the Euler-Lagrange equations.

Despite being very intuitive, snakes suffer from the following numerical issues [15]:

1. They are sensitive to initialization.
2. They don’t work well with noisy data, which can be a significant issue in real-world scenarios where data may be incomplete or corrupted.
3. Use of snake require sophisticated numerical methods [16, 17, 18, 19] to solve Euler-Lagrange equations.
4. Hyperparameter tuning can be challenging, as selecting optimal parameters for the model can be time-consuming and require significant expertise.
5. Snakes can’t handle topology changes, which occur when objects in the image intersect or touch.
6. It is difficult to incorporate prior domain knowledge in the form of energy functionals, which can limit the model’s ability to leverage existing domain knowledge.

In this work, we propose PICS (Physics Informed Contour Selection) that integrates snakes and PINNs in a manner that capitalizes on the strengths of both approaches while mitigating their weaknesses. To accomplish this, we modified the PINN approach by introducing the following novelties:

- *Custom design the PINN hypothesis (network architecture) to effectively capture object boundaries.* PINNs use a deep neural network (see eq.6) with a large number of parameters to approximate the solution, whereas PICS employs cubic splines (see eq.11) that can efficiently approximate any closed contour with only a few control knots. The use of a simplified architecture leads to significant speed ups as compared to traditional PINNs[4, 7, 20, 21].
- *Assign control knots as a design variable.* In most deep neural networks, the weights are typically initialized randomly and do not have any physical significance. However, PICS is formulated in such a way that trainable weights are represented by the control knots of cubic splines. It gives it a clear physical meaning to weights that simplifies scaling and normalization steps. Similarly, the loss gradient in PICS can be physically interpreted as the *force* on the control knots pushing them towards the direction of gradient descent.
- *Minimize region-based loss instead of gradient-based loss functionals.* PICS enhances the stability of snakes towards noisy data by optimizing region-based energy functionals [22, 23] instead of relying solely on edge-based energy functionals [14, 16, 17, 19]. This approach has never been attempted in traditional numerical or deep learning frameworks because there is no explicit differentiable function for the derivative of the region-based loss with respect to snake control knots. We are the first to address this issue by implicitly calculating the loss derivatives through finite difference methods.
- *Incorporate prior shape information via regularization terms.* Like the parent PINN, PICS can easily accommodate any prior information about the shape of the object via shape-based regularization terms.
- *Exploit transfer learning for 3D segmentation.* Given multiple 2D slices of a 3D object, PICS exploits transfer learning to reuse the optimized weights (spline control knots) from the previous slice as the initial condition for segmenting the current slice. This modality allows the snake to quickly converge to the optimal segmentation for each slice, reducing the number of iterations required for convergence and the overall computational cost.

To demonstrate the effectiveness of PICS, we take an example from the field of medical image segmentation. Medical image segmentation is a critical step in disease diagnosis, treatment planning, and medical research[24, 25, 26, 27]. This process involves locating the regions of interest from medical images, such as magnetic resonance imaging (MRI) or computerized tomography (CT) scans, which can be used to identify and diagnose abnormalities, tumors, and other medical conditions. In recent years, medical image segmentation has been revolutionized by the rapid development of deep learning algorithms for computer vision[28, 29, 30]. These algorithms have shown impressive results[31, 32, 33, 34, 35, 36] in accurately segmenting medical images, thus improving the accuracy and efficiency of medical diagnosis and treatment. However, their success heavily depends on the quality and quantity of the training data[37, 38, 39]. The problem is that acquiring high-quality medical images with labels (also called masks) requires expert interpretation [40], and it is a labor-intensive and time-consuming process[41, 42]. Furthermore, the automatic tools are not trusted[43] within the medical community. Therefore, PICS can fill a crucial research gap by serving as an intuitive tool for medical practitioners to generate rapid annotations, addressing the limitations associated with acquiring labeled medical images and improving the efficiency of the segmentation process.

The organization of this paper is as follows. We start with a brief review of snakes and PINN. Next, we list the objectives of the paper. In the Methods section, we describe the mathematical formulation of PICS. Then, we discuss the results in Results section. Finally, the conclusions of the paper are given at the end.

2 Brief Review of Snake and PINN

2.1 Brief Review of Snake Model

Consider Fig.1 in which the snake (or deformable contour) has maximum energy at the start, and following the minimization process, it converges to the object's boundary. Mathematically, if the total energy of the snake is given by

$$J = \frac{\alpha}{2} \int_0^1 \psi_s^2 ds + \frac{\beta}{2} \int_0^1 \psi_{ss}^2 ds + J_{ext} \quad (1)$$

where (s, t) denote space and time parameters respectively, ψ denotes the parametric spline used for segmentation contour, (α, β) are the coefficients, the sum of first two terms denotes the internal energy (J_{int}) of the snake and J_{ext} denotes external energy.

Then, the motion of the snake is governed by the following PDE:

$$\frac{\partial \vec{\psi}}{\partial t} = \alpha \frac{\partial^2 \vec{\psi}}{\partial s^2} + \beta \frac{\partial^4 \vec{\psi}}{\partial s^4} - \nabla J_{ext} \quad (2)$$

The internal energy controls the smoothness of snake and it is independent of the data. However, J_{ext} is an image dependent, edge-based functional. For example, if I is the image, then a simple gradient-based J_{ext} could be $J_{ext} = -\int_0^1 |\nabla I|^2 ds$. For such functionals, a differentiable function for the gradient of J_{ext} with respect to control knots cannot be found. However, if J_{ext} is a region-based functional (for example, refer equation 16), then the expression for ∇J_{ext} with respect to control knots cannot be directly found. If the object has weak gradients and the image is noisy, the denoising also removes the object boundary. In such cases, region-based loss functions are beneficial, but the traditional snake framework is not suitable for their implementation.

2.2 Brief Review of PINNs

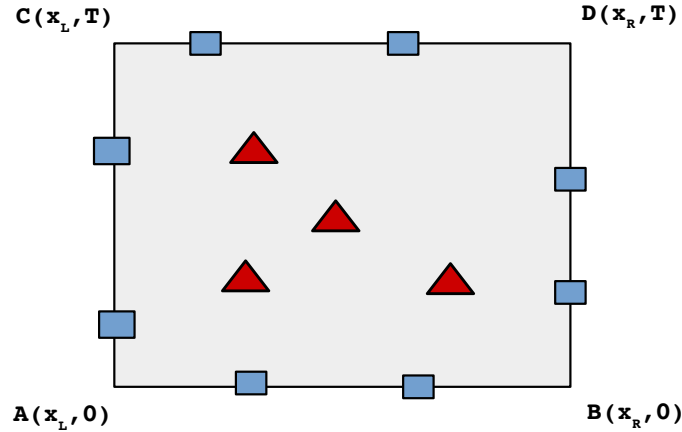


Figure 2: Distribution of collocation (red triangles) and boundary points (blue rectangles) in the computational domain.

In a typical PINN, the solution of PDE is approximated by a deep neural network. The training data, which consists of collocation and boundary points (see Fig.2), are randomly distributed in the computational domain. For example, consider the following one-dimensional (1D) unsteady PDE.

$$\frac{\partial}{\partial t} u(x, t) + Nu(x, t) = R(x, t), (x, t) \in \Omega \quad (3)$$

$$u(x, t) = B(x, t), (x, t) \in \partial\Omega, \quad (4)$$

$$u(x, 0) = F(x), x \in (x_L, x_R), \quad (5)$$

where \mathcal{N} is a nonlinear differential operator and $\partial\Omega$ is the boundary of the computational domain Ω . We approximate u with a n -layered deep neural network ψ such that

$$\psi = \psi(z; W_1, W_2 \dots W_n, b_1, b_2, \dots b_n) = W_n(\dots(\phi(W_2(\phi(W_1 z + b_1))) + b_2)) \dots) + b_n \quad (6)$$

where $z = [x, t]^T$ denote sampling points, (W_i, b_i) denote model parameters and ϕ denotes nonlinearity. For PINNs, z are randomly selected, but after selection, they remain fixed. If we denote the errors in approximating the PDE, BCs, and IC by $\vec{\xi}_f$, $\vec{\xi}_{bc}$ and $\vec{\xi}_{ic}$ respectively. Then, the expressions for these errors are as follows:

$$\vec{\xi}_f = \frac{\partial \vec{\psi}}{\partial t} + \mathcal{N}\vec{\psi} - \vec{R}, \text{ on } (\vec{x}_f, \vec{y}_f) \quad (7)$$

$$\vec{\xi}_{bc} = \vec{\psi} - \vec{B}, (\vec{x}_{bc}, \vec{t}_{bc})_{side\ faces} \quad (8)$$

$$\vec{\xi}_{ic} = \vec{\psi}(\cdot, 0) - \vec{F}, (\vec{x}_{bc}, \vec{t}_{bc})_{bottom\ face} \quad (9)$$

For shallow networks, $\frac{\partial \vec{\psi}}{\partial t}$ and $\mathcal{N}\vec{\psi}$ can be determined using hand calculations. However, for deep networks, we have to use finite difference methods or automatic differentiation [44]. The latter is preferred for its computational efficiency. We can recast the PDE, BC, IC system to an optimization problem by minimizing an appropriate loss function. The loss function J to be minimized for a PINN is given by

$$J = \frac{\vec{\xi}_f^T \vec{\xi}_f}{2N_f} + \frac{\vec{\xi}_{bc}^T \vec{\xi}_{bc}}{2N_{bc}} + \frac{\vec{\xi}_{ic}^T \vec{\xi}_{ic}}{2N_{ic}}, \quad (10)$$

where N_f , N_{bc} , and N_{ic} refer to the number of collocation points, boundary condition points in left and right faces, and initial condition points at the bottom face, respectively. We can see that we have chosen a least square loss function. Now, any gradient based optimization routine may be used to minimize J .

3 Objectives

The objective of the paper is to demonstrate the effectiveness of the PICS in performing image segmentation in both 2D and 3D settings, with and without prior knowledge of the object's shape. Specifically speaking,

1. Given a 2D image, perform segmentation with and without prior shape information.
2. Given a 3D image, perform segmentation with and without prior shape information.
3. Discuss hyperparameter tuning for simple and complex images.

Furthermore, the paper aims to evaluate the performance of the method against labeled data to assess its accuracy and reliability.

4 Methods

Figure 3 shows the overall flowchart of PICS. In this section, we will describe its individual components, i.e., (a) PICS hypothesis, (b) the Chan-Vese loss function, (c) optimization, (d) the prior shape-based loss term, and (e) the operation performance index (OPI)—a metric to monitor the optimization performance of PICS.

4.1 PICS Hypothesis

We approximate the solution in PICS, i.e., object boundary with a parametric spline. The expression of parametric spline $\vec{\psi}$ is given by

$$\vec{\psi}(s) = \begin{cases} \vec{\psi}_1 & s_1 < s < s_2 \\ \vec{\psi}_2 & s_2 < s < s_3 \\ \dots & \dots \\ \vec{\psi}_n & s_n < s < s_1 \end{cases} \quad (11)$$

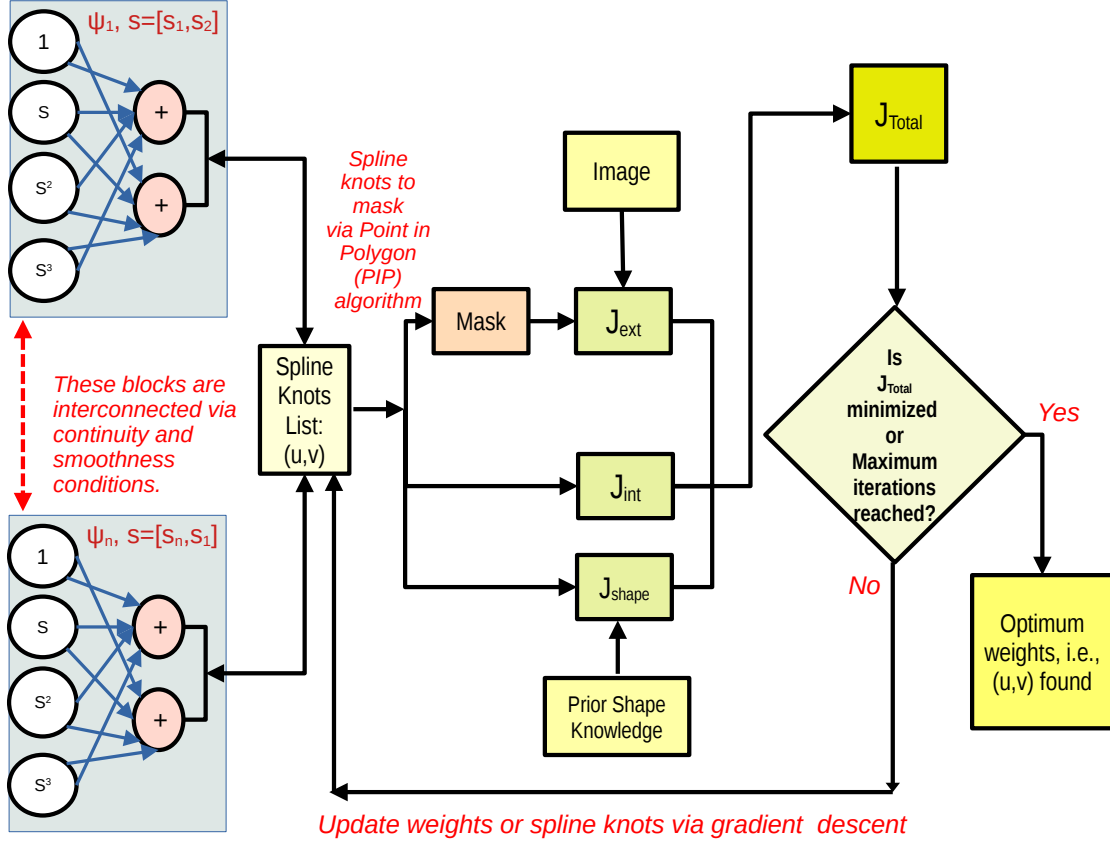


Figure 3: Overview of PICS algorithm.

where the local cubic spline $\vec{\psi}_i(s_i < s < s_{i+1})$ is given by

$$\vec{\psi}_i(s) = \begin{Bmatrix} u_i(s) \\ v_i(s) \end{Bmatrix} = \begin{Bmatrix} a_i s^3 + b_i s^2 + c_i s + d_i \\ e_i s^3 + f_i s^2 + g_i s + h_i \end{Bmatrix} \quad (12)$$

In the given equation, s is a parameter that varies from 0 to 1. $[u_i, v_i]'$ denotes the spatial coordinates of the local spline ψ_i . For given $[u_i, v_i]'$, the coefficients of local splines, denoted by $[a_i, b_i, \dots, h_i]'$, are computed by satisfying the conditions of continuity, smoothness, and periodicity.

It is important to note that unlike in PINN (recall eq. 6), these spline coefficients are not directly considered trainable weights in PICS. *In PICS, the weights are the sampling points or the control knots themselves, i.e., $[u_i, v_i]'$.* With respect to Fig. 3, we do not start with the left most blocks which represent local cubic splines. Our starting point is the list of spline knots. The spline coefficients are back calculated by a simple matrix operation. This novelty brings physical interpretability to the trainable parameters which otherwise don't have any direct physical significance.

Furthermore, PICS does not require any batch normalization as the physical constraints of continuity, smoothness, and periodicity, i.e., scale its weights,

1. Continuity: $\vec{\psi}_{k-1}(s_k) = \vec{\psi}_k(s_k) = \begin{Bmatrix} \tilde{u}(s_k) \\ \tilde{v}(s_k) \end{Bmatrix}$
2. Smoothness: $\frac{d}{ds} \vec{\psi}_{k-1}(s_k) = \frac{d}{ds} \vec{\psi}_k(s_k)$ and $\frac{d^2}{ds^2} \vec{\psi}_{k-1}(s_k) = \frac{d^2}{ds^2} \vec{\psi}_k(s_k)$
3. Periodicity: $\frac{d}{ds} \vec{\psi}_n(s_n) = \frac{d}{ds} \vec{\psi}_1(s_1)$ and $\frac{d^2}{ds^2} \vec{\psi}_n(s_n) = \frac{d^2}{ds^2} \vec{\psi}_1(s_1)$

4.2 Loss Function and Optimization

The formula for the region-based [22, 23] loss function is given by

$$J = \alpha J_{\psi_s} + \beta J_{\psi_{ss}} + \mu J_{cv} \quad (13)$$

where

$$J_{\psi_s} = \sum_{i=1}^{i=N} \frac{1}{N} \left(\left(\frac{d\tilde{u}}{ds} \right)^2 + \left(\frac{d\tilde{v}}{ds} \right)^2 \right)_i \quad (14)$$

$$J_{\psi_{ss}} = \sum_{i=1}^{i=N} \frac{1}{N} \left(\left(\frac{d^2\tilde{u}}{ds^2} \right)^2 + \left(\frac{d^2\tilde{v}}{ds^2} \right)^2 \right)_i \quad (15)$$

$$J_{cv} = \sum_{q=1}^{q=N_y} \sum_{p=1}^{p=N_x} ((I(p, q) - \mu_{in}) \chi(p, q))^2 + \gamma (\nabla I(p, q) \chi(p, q))^2 + ((I(p, q) - \mu_{out}) (1 - \chi(p, q)))^2 \quad (16)$$

In the above expressions, I denotes the image, (\tilde{u}, \tilde{v}) denotes spline knots, and N denotes the number of spline control knots. χ denotes a characteristic function or mask that is generated by repeated geometric queries, that is, given a single polygon through spline knots and a sequence of query points (grid points), find if the query point lies inside or outside the polygon using point in polygon algorithms [45]. μ_{in}, μ_{out} denote the average pixel value of the image within and outside the spline contour. N_x, N_y denote number of pixels in x and y direction respectively. With respect to Fig. 3, the external energy term of the loss is $J_{ext} = \mu J_{cv}$, and the internal energy term is $J_{int} = \alpha J_{\psi_s} + \beta J_{\psi_{ss}}$. The hyperparameter γ aims to make the pixel intensities inside the contour more uniform.

While doing the weight update by gradient descent, the derivative of loss with respect to weights is compulsory. For example, The expression for weight update using gradient descent is given by

$$w = w_{old} - \lambda \frac{\partial J}{\partial w_{old}} \quad (17)$$

where w denotes weight or spline control knots, λ is the learning rate and $\frac{\partial J}{\partial w}$ is the loss gradient. The loss gradient cannot be calculated directly or even by automatic differentiation because there is no explicit differentiable function that maps control knots with mask. Therefore to calculate derivatives, we use central difference scheme. This is the advantage of minimizing the energy functional instead of using PINN-like PDE residual, as it relaxes the differentiability requirements. For faster convergence and adaptive learning rate, we have used Adam [46] optimizer for our numerical experiments.

4.3 Prior Shape-Based Loss Term

This paper will use PICS to generate annotations for the left ventricle in the cardiac MRI scan images. A representative cardiac MRI scan shown in the left-hand side of Figure 4 is composed of three main parts: left ventricle, right ventricle, and myocardium. In clinical applications of cardiac left ventricle (LV) segmentation, it is desirable to include the cavity, trabeculae, and papillary muscles, which collectively form a convex shape, as shown by the right-hand side of Figure 4 where some reference annotations for left ventricle are depicted. However, trabeculae and papillary muscles have similar intensities to the myocardium, which can cause segmentation algorithms to incorrectly classify them as myocardium.

The problem here is to find a way to accommodate medical domain knowledge with a purely data or image-driven algorithm. To address this challenge, Shi and Li [47] developed a method that preserves the convexity of the left ventricle by controlling the curvature in the level set framework. Similarly, in PICS, we propose a new loss term that preserves convexity in the snake framework. This loss term is expressed as follows:

$$J_{shape} = \sigma \sum_{i=1}^{i=N} \frac{1}{N} \kappa^2 = \sigma \sum_{i=1}^{i=N} \frac{1}{N} \left(\frac{\tilde{v}_{ss}\tilde{u}_s - \tilde{u}_{ss}\tilde{v}_s}{(\tilde{u}_s^2 + \tilde{v}_s^2)^{\frac{3}{2}}} \right)^2 \quad (18)$$

where κ denotes the curvature of contour, N denotes number of spline control knots and σ is a hyperparameter. This penalty term ensures that the shape of the predicted boundary remains convex-shaped. Please note that such an information about the shape of the object is not always available. In those cases, as Fig. 3 shows, PICS works with just J_{int} and J_{ext} .

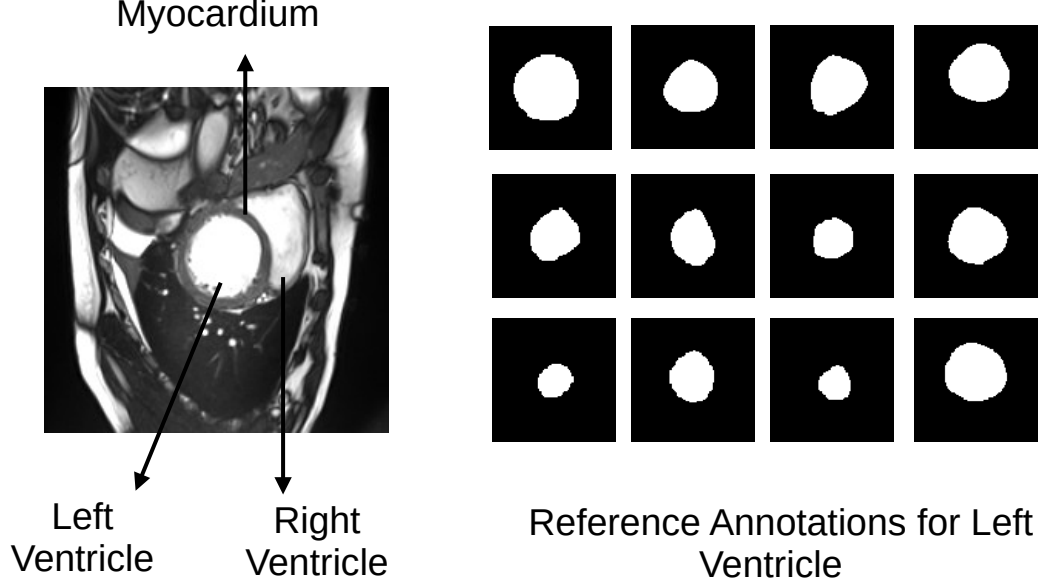


Figure 4: Description of the cardiac dataset and sample annotations for the left ventricle.

4.4 Operation Performance Index (OPI)

The region-based loss function is comprised of both shape regularization and external energy (or mean square error) terms. During optimization, our aim is to reduce the total loss. However, if the relative strengths of the shape regularization and MSE terms need to be appropriately balanced, the solution may get stuck in a local minimum.

To prevent this issue, we introduce a new performance evaluation metric known as the Operation Performance Index (OPI). A value of one for OPI indicates that PICS is moving in the right direction, while a value below a predetermined threshold (e.g., 0.8) indicates that parameter adjustments are necessary. However, what constitutes the "right direction"? In the best-case scenario, both external and internal energies should drop as optimization proceeds. However, if that is not possible, the external energy should always drop whether shape regularization loss drops or not. This idea is mathematically contained in the following formula for OPI:

$$OPI_k = 1 - \frac{\langle \vec{\theta}_k, \vec{P}_k \rangle}{2 \sum \theta_k} \quad (19)$$

where

$$\begin{aligned} \vec{P}_k &= \text{sign}(\Delta J_{int}(k-w+1:k)) - \text{sign}(\Delta J_{ext}(k-w+1:k)) \\ \vec{\theta}_k &= \frac{\exp([1, 1+d, \dots, 1+id, \dots, 2])}{\sum_{i=0}^{w-1} \exp(1+id)}, d = \frac{1}{w-1} \end{aligned}$$

k , w and $\langle \rangle$ represent iteration number, iteration window size, and dot product, respectively. ΔJ represents vector of difference in J . The exponential smoothing term ensures that the recent values are given more weightage.

OPI can also be used for hyperparameter tuning. For instance, the values of the hyperparameters α and β can be determined through trial and error. But, the third parameter, μ , which is initially set to $1e3$, can be adjusted using OPI. When OPI falls below the threshold, the update rule for μ is given by

$$\mu = \mu + 2^{\log_{10}(J_{ext}/J_{int})} \quad (20)$$

However, we do not continue adjusting μ indefinitely. We stop adjusting μ once the order of J_{ext} becomes more than $1e4$ times that of J_{int} to prevent the snake from becoming too loose.

When examining the total loss history alone, it is difficult to determine whether the optimization is progressing correctly. However, looking at the OPI trend, we can check if its value is very low or wildly fluctuating between 0 and 1. Based on this information, the hyperparameters may be adjusted. We will cover the application of this idea in the next section.

We summarize this section with two tables. Table 1 lists the similarities and differences between PICS and PINNs, and Table 2 lists the problems with snake model and their remedies in PICS.

Property	PINN	PICS
Basis function	Deep neural network (nonlinear)	Cubic splines (linear)
Parameters	Weights and biases (no physical interpretation)	Control knots (interpretable)
The gradient of loss with respect to parameters	No physical interpretation	Force on the control knots
Training Points	Scattered points (mesh-free)	Scattered points (mesh-free)
PDE embedding	PDE as loss function	PDE functional as loss function
Optimization	Gradient-based	Gradient-based

Table 1: Comparison between PINN and PICS.

5 Results and Discussion

In this section, we demonstrate the effectiveness of PICS in 2D and 3D segmentation with and without prior shape information. In all the cases, Adam optimizer [46] is used. All the experiments are conducted in Matlab R2022b environment running in a 12th Gen Intel(R) Core(TM) i7-12700H, 2.30 GHz CPU and 16GB RAM Asus laptop. For testing PICS, we have considered the following cases:

1. CT scan of enlarged ventricles of hydrocephalus patient (Case courtesy of Paul Simkin, Radiopaedia.org, rID: 30453). The source of data is: <https://radiopaedia.org/cases/obstructive-hydrocephalus>
2. Synthetic image of a disk with distorted boundaries. This test case was also used by Xie et al. [17].
3. Synthetic image of a cavity [16, 17, 18]. This is a standard test case where traditional snake models have been observed to be unsuccessful in navigating through concavities.
4. MRI scans of cardiac data of 100 patients from the ACDC dataset[48] in the ED, i.e., End-Diastolic phase. Source:<https://www.creatis.insa-lyon.fr/Challenge/acdc/index.html>

The first three tests can be assessed visually without the need for prior shape information. However, the last test, which uses the ACDC dataset, requires expert interpretation and therefore is evaluated by comparing the results with annotations provided by medical professionals. The intersection over union (IoU) is used as the evaluation metric to

S.No.	Snake problem	PICS solution
1	Sensitive to initialization	Physically consistent initialization by humans
2	Sensitive to noisy data	Robust to noisy data due to use of region-based functionals
3	Requires sophisticated algorithms to solve Euler-Lagrange equations	Requires simple gradient-descent for all kind of loss functionals
4	Difficult to incorporate shape-priors	Easy to incorporate shape-priors as loss functions
5	Only forward problems	Forward as well as inverse problems

Table 2: PICS solution for snake problems.

compare the results. IoU measures the similarity between two sets of data by dividing the size of their intersection by the size of their union. The formula for IoU is:

$$IoU(A, B) = \frac{|A \cap B|}{|A \cup B|}$$

where A and B are the two sets being compared. The IoU value ranges from 0 to 1, where 0 indicates no common elements between the sets and 1 indicates identical sets.

5.1 2D image segmentation without any prior shape information

In this case, we consider a CT scan of the enlarged ventricles of a hydrocephalus patient. Figure 5 shows the segmentation results. The CT scan shows two enlarged ventricles. The left-hand side of Figure 5 shows the contours initialized by the PICS user, and the right-hand side figure shows the optimized weights. By visual inspection, we can conclude that the results are satisfactory. The number of trainable parameters (i.e., two times the control knots) N equals 22. The values of hyperparameters used are: $(\alpha, \beta, \mu, \gamma, \sigma) = (5e-1, 5e-2, 1e3, 0, 0)$. The values of α and β are fixed by trial and error. The value of μ is adaptive depending on the OPI discussed earlier. The time taken during the optimization process is close to a minute. Therefore, PICS shows good performance when dealing with images that contain a single target object or when the number of target objects is known.

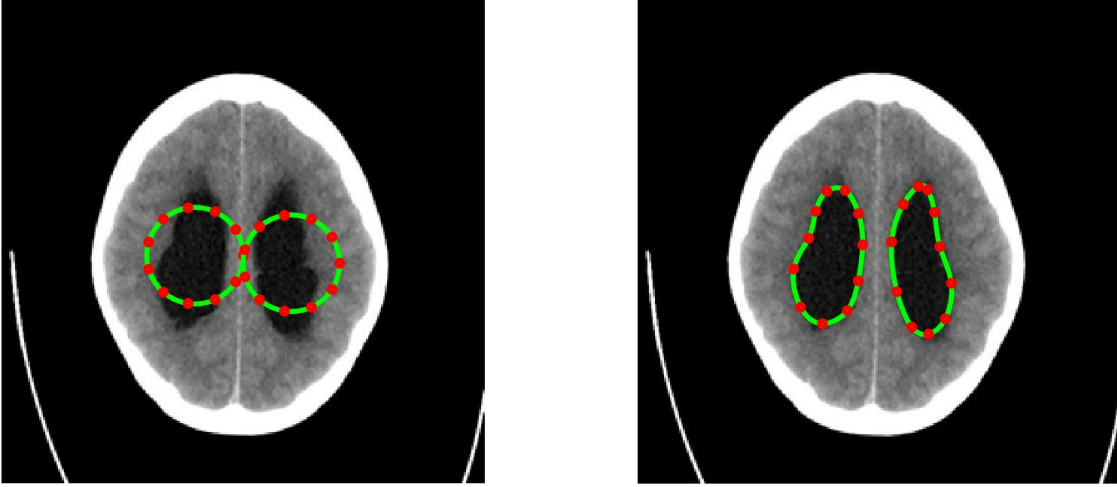


Figure 5: segmentation of enlarged ventricles of a hydrocephalus patient. Left: Initial weights, Right: Optimized weights.

5.2 2D image segmentation with prior shape information

In this case, we consider the synthetic image of a disk with distorted boundaries. Figure 6 shows the segmentation results without and with shape prior. The synthetic disk has a partially distorted boundary. The left-hand side of Figure 6 shows the contours initialized by the PICS user. The middle figure shows the segmentation result without the shape loss term. The right-hand side figure shows the segmentation result with the shape loss term. The number of trainable parameters (i.e., two times the control knots) N equals 30. The values of hyperparameters without shape loss term are: $(\alpha, \beta, \mu, \gamma, \sigma) = (5e-1, 1e-2, 1e4, 0, 0)$ and with shape prior are $(\alpha, \beta, \mu, \gamma, \sigma) = (5e-1, 1e-2, 1e4, 0, 1e8)$. The values of σ are fixed by trial and error. Therefore, the inclusion of a shape loss term enables PICS to nearly recover the original shape of an object even when the boundary is distorted.

5.3 3D image segmentation with or without prior shape information

- *Effect of inclusion of convexity preserving loss term in LV segmentation.* Figures 7 and 8 demonstrate the impact of integrating a convexity-preserving loss term in the segmentation of the left ventricle for the ED (End-diastolic) case. As depicted in the middle figure, a purely data-driven segmentation algorithm is likely to fail in cases where trabeculae and papillary muscles have comparable intensities to the myocardium. However, by incorporating prior shape information that preserves convexity, PICS is able to accurately segment the left ventricle even in the presence of confusing muscles. The inclusion of the shape loss term results in an increase

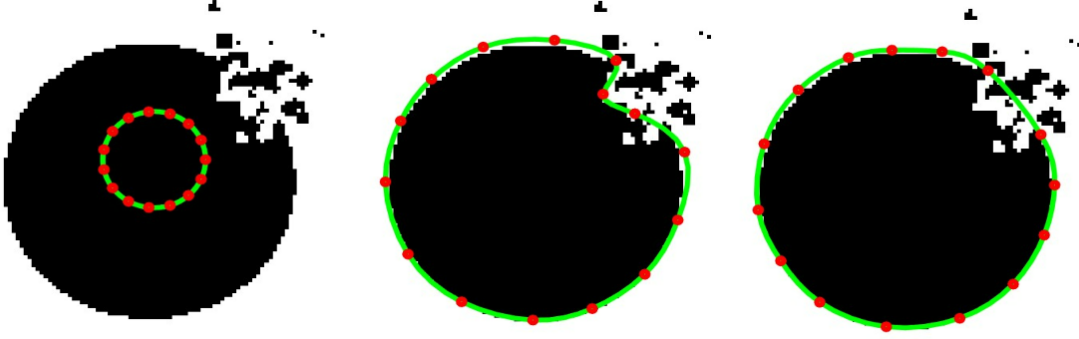


Figure 6: Effect of inclusion of convexity preserving loss term in 2D segmentation. Left: Initial weights, Middle: Optimized weights without shape prior, Right: Optimized weights with shape prior.

of the IoU score from 0.49 without the shape loss term to 0.87 with it. The values of hyperparameters without and with shape loss term are $(\alpha, \beta, \mu, \gamma, \sigma) = (5e-1, 1e-3, 1e4, 0, 0)$ and $(5e-1, 1e-3, 1e4, 0, 1e8)$ respectively. The number of trainable weights in both cases is 20.

- *Rapid 3D segmentation via transfer learning.* If F represents a nonlinear transformation that takes image $I(x, y)$ and initial weights \vec{w} as input and gives weight update as output. We can model the 3D segmentation process as follows:

$$\vec{w}^{[n]} = \vec{w}_{opt}^{[n-1]} + F(I(x, y)^{[n]}, \vec{w}_{opt}^{[n-1]}), n = 1, 2, 3, \dots \quad (21)$$

where the weights are initialized by a single mouse click of the user, i.e.,

$$\vec{w}^{[0]} = \vec{w}_{user} \quad (22)$$

It is mathematically equivalent to solving an unsteady PDE given by

$$\frac{d\vec{w}}{dt} = F(I(x, y), \vec{w}) \quad (23)$$

Figure 9 demonstrates the 3D segmentation process of the left ventricle in the PICS framework. The initialization process begins with a single click within the left ventricle on the first MRI image. Subsequently, the optimal PIC weights obtained from the previous image are transferred as the initial condition for the next image. The transfer learning accelerates the convergence of the PIC to its optimal value. This iterative process is continued for all the remaining images. Figure 10 illustrates an example of the speed-up in convergence due to this transfer learning process.

- *Performance evaluation on ACDC dataset.* Figure 11 shows the performance of PICS on all the hundred patients' data, with an average IoU of 0.88. The probability mass function is also shown. The number of trainable parameters for all the cases is the same, which is 20 parameters. However, the choice of hyperparameters is not the same for all cases. Based on the images in the ACDC dataset, they can be broadly categorized into three classes (see Figure 12): (1) Normal Case, (2) Indistinct Muscles, and (3) Very Thin Myocardium. PICS uses different hyperparameter settings for different image categories in the ACDC dataset. For the normal case, the hyperparameters have values of $(\alpha, \beta, \mu, \gamma, \sigma) = (1e-1, 1e-2, 1e4, 1e-5, 1e7)$. For the indistinct muscles category, the value of σ is increased by a factor of 10 while keeping all other hyperparameters fixed. Similarly, for the last class with very thin myocardium, the value of γ is increased by a factor of 100-200 while keeping all other hyperparameters fixed. These hyperparameter settings are based on the observations from the ACDC dataset and have been found to provide good performance in their respective image categories.

Comparison with winners of ACDC challenge. First and foremost, it's important to recognize that comparing PICS with a deep learning-based segmentation algorithm isn't entirely fair because PICS creates annotations (ground truth), while neural networks make predictions. The best IoU score (<https://www.creatis.insa-lyon.fr/Challenge/acdc/results.html>) is 0.96 while ours is 0.88. Despite the fact that our result (IoU=0.88) places us at the bottom of the leaderboard, it's still a promising result when compared to traditional deep neural networks which are complex, with millions of parameters, requiring extensive training sessions lasting several hours and a substantial amount of high-quality data for effective training.

The annotations generated by PICS can serve as a preliminary mask for the labeler, who can then refine them by correcting the positions of control knots as needed. From an algorithmic perspective, this refinement can be accomplished by fixing the satisfactory control knots or weights as "non-trainable" and allowing the remaining ones to adjust. Within the scope of this discussion, the results obtained in our current study, which serves as an initial proof of concept, are very promising.

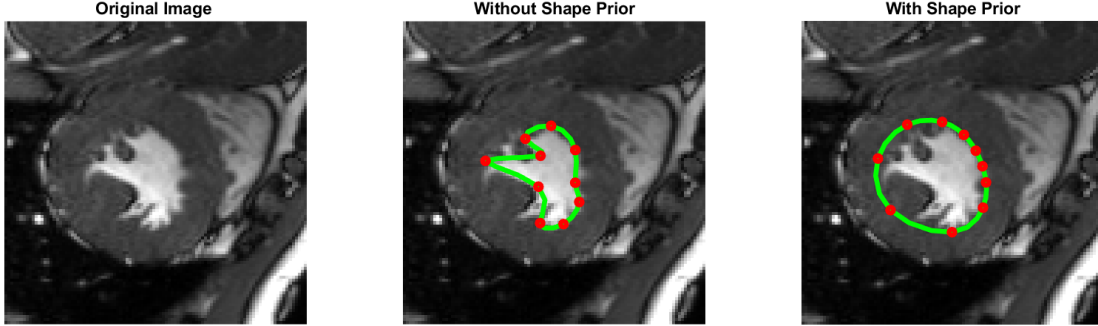


Figure 7: Effect of inclusion of convexity preserving shape prior in segmentation (control knots) of the left ventricle.

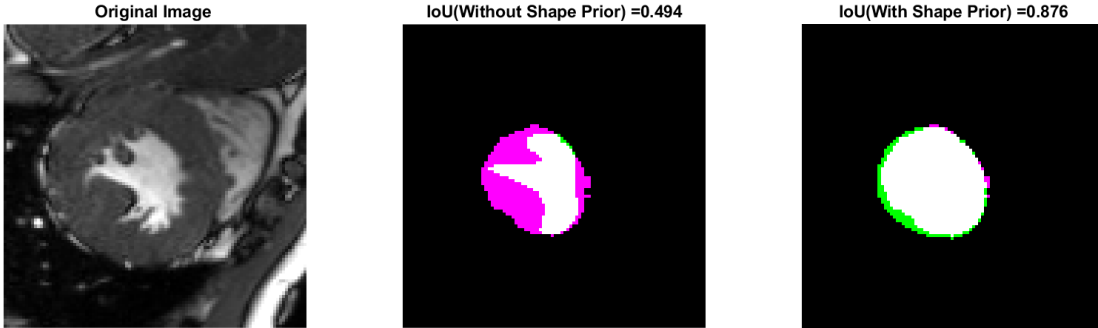


Figure 8: Effect of inclusion of convexity preserving shape prior in segmentation (masks) of the left ventricle.

• **Limitation of PICS**

1. *Inverse parameter estimation.* It may be argued that because PINNs have been successful in both forward and inverse problems and PICS is derived from PINN, it should be possible to estimate hyperparameters by minimizing a loss function with hyperparameters treated as trainable weights. However, Zapf *et al.* [49] explain that this may not be effective. Even when the predicted segmentation is correct, all three terms of the PICS loss function, including shape regularization, region-based loss, and shape-based loss, may not be equal to zero. Depending on the image complexity, the ratio of region-based loss to other losses may be the most trustworthy at times, while the ratio of shape-based loss to others may be most trustworthy at other times. Therefore, in this work, hyperparameters were chosen through trial and error. For simpler images, like those in Figure 17, we can select the ratio of region-based loss to other losses as the most trustworthy and automate the hyperparameter selection process. Readers can appreciate that the proposed OPI effectively implements the suggestion by Zapf *et al.* [49].
2. *Topology change.* The PICS framework for 3D segmentation has a limitation regarding images that change topology during segmentation. In such cases, multiple initializations are required, but the number of initializations needed is fixed based on the topology of the first image. This limitation is demonstrated in Figure 13, where the 3D segmentation of CT scans of a hydrocephalus patient starts with one object in the first image but breaks into two parts in the fourth image, causing PICS to struggle with the increased number of parts. This issue may affect the accuracy and efficiency of the segmentation in cases where topology changes occur frequently.
3. *Less number of heart section images.* If there are only a few slices available for a specific cardiac cycle phase, such as end-diastole (ED), it could result in a significant change in the size of the left ventricle across adjacent slices, which can affect the accuracy of segmentation. Hence, having a larger number of slices available for a given phase is better for accurate segmentation of the left ventricle.

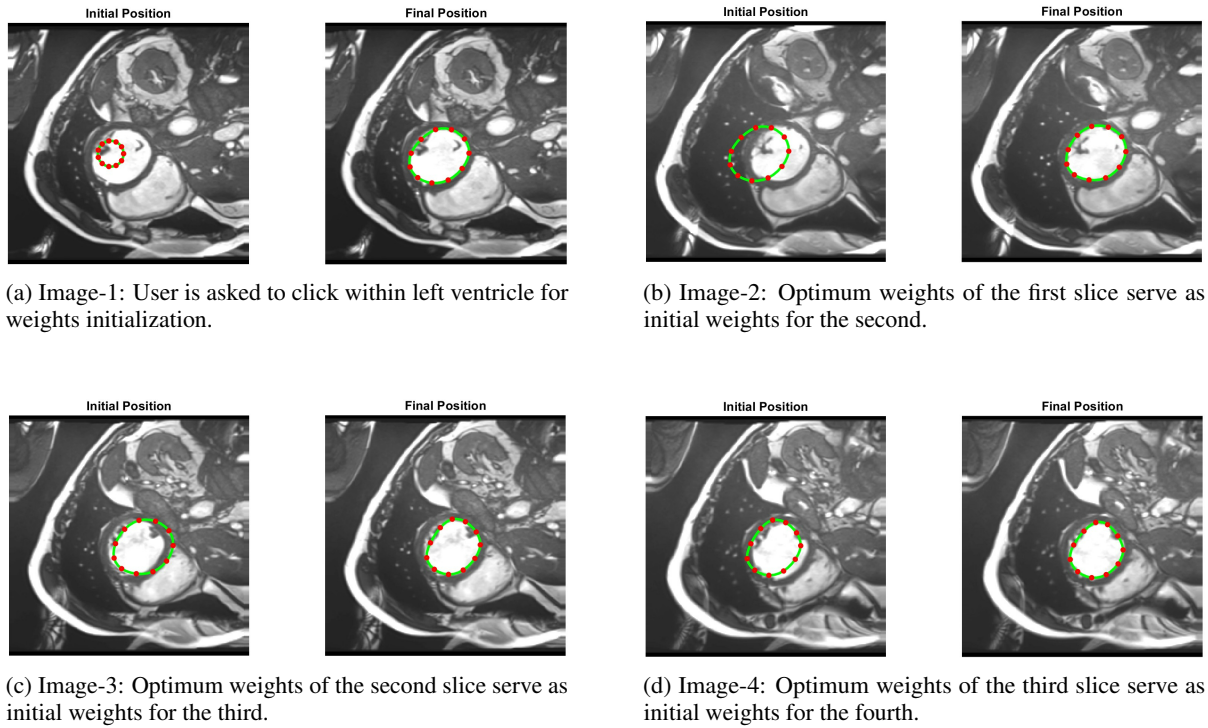


Figure 9: 3D segmentation of left ventricle with PICS using transfer learning (for ED phase).

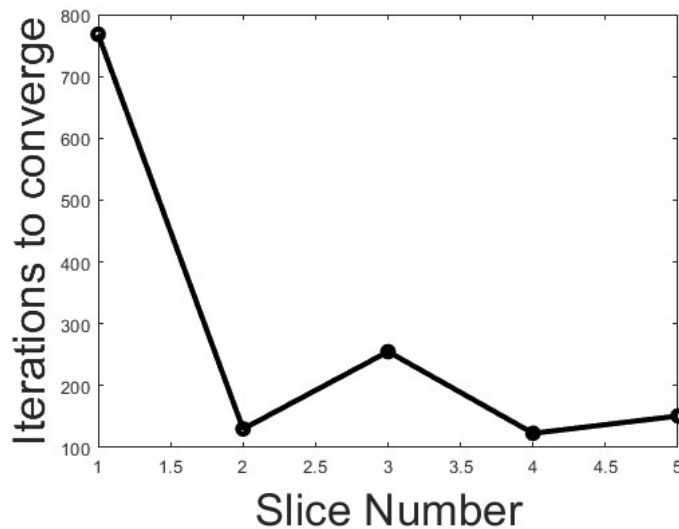


Figure 10: Faster convergence due to transfer learning.

5.4 Adaptive hyperparameter tuning with OPI

- *A global minimum and a local minimum.* Figure 14 displays two instances of bad minima. The first example shows a shrunken snake due to a high value of the bending coefficient. In contrast, the second shows the snake getting trapped in a local minimum because the increase in loss value caused by extension is greater than the drop in loss value due to the Chan-Vese loss. The loss history and OPI trend for each case are shown in Figures 15 and 16 respectively. When examining the total loss history alone, it is difficult to determine whether the optimization is progressing correctly. However, looking at the OPI trend, we can see that its value is zero for the first case and fluctuates wildly between 0 and 1 for the second. Therefore, we can rely on the OPI to

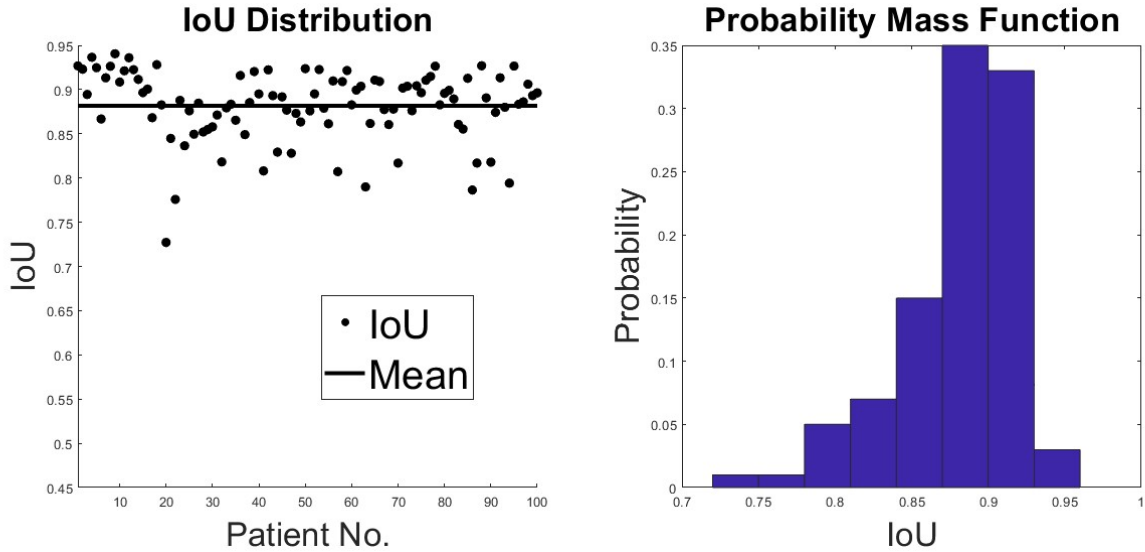


Figure 11: Performance of PICS in annotating the whole dataset consisting of 100 patients.

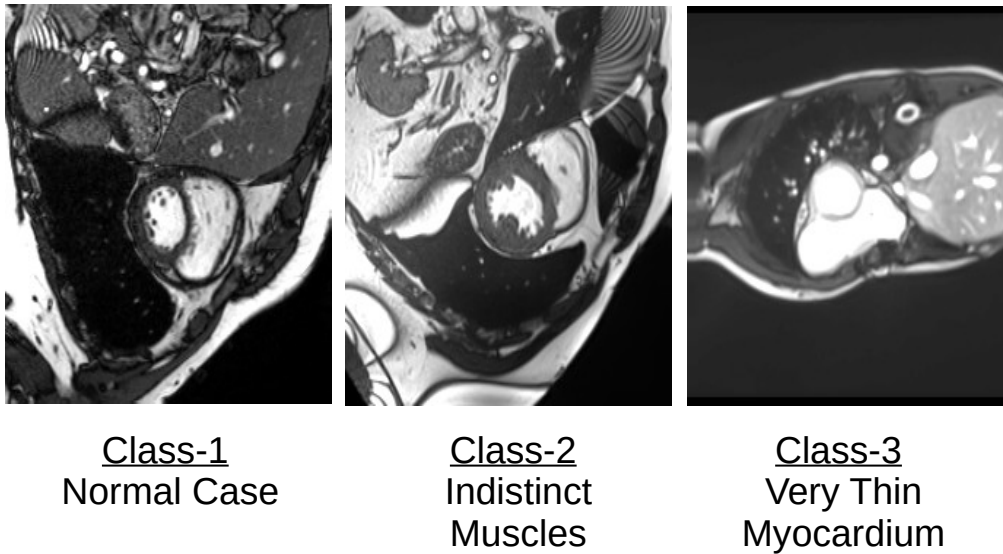


Figure 12: Hyperparameter selection for three distinct classes.

determine that PICS is stuck in a local minimum and requires adjustments to its hyperparameters to overcome this issue.

- *Adaptive hyperparameter tuning.* Figure 17 demonstrates that PICS is capable of accurately capturing concave regions. Figures 18 and 19 provide additional information on this particular case, including the OPI score, loss history, and adaptive tuning of hyperparameters. Similar results are shown in the figs.20 and 21. In this case, we segment Texas state borders from the USA map. These figures show that hyperparameters are adjusted as

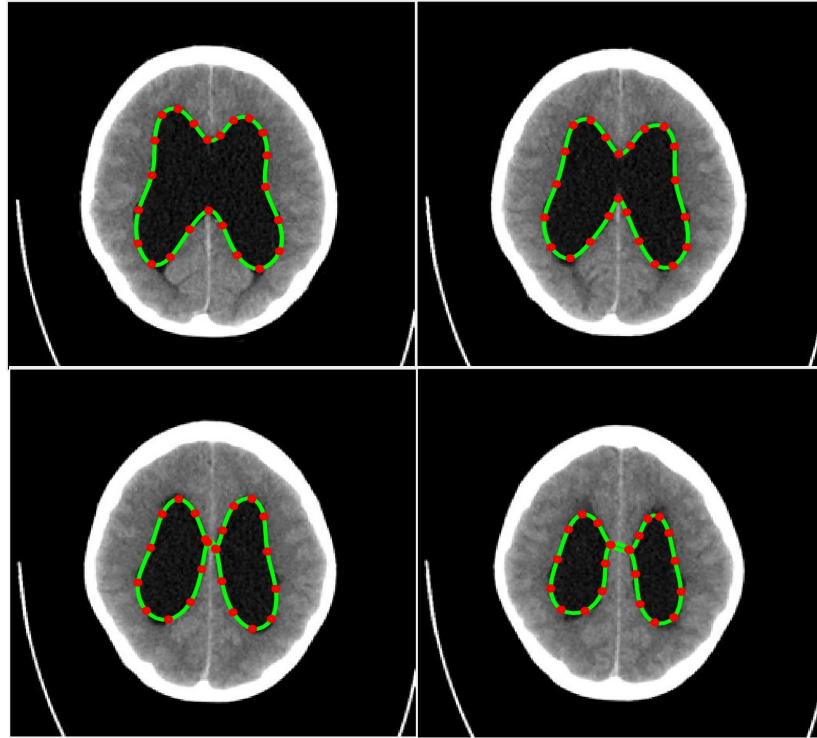


Figure 13: An example of topology change: 3D segmentation of enlarged ventricles of a hydrocephalus patient.

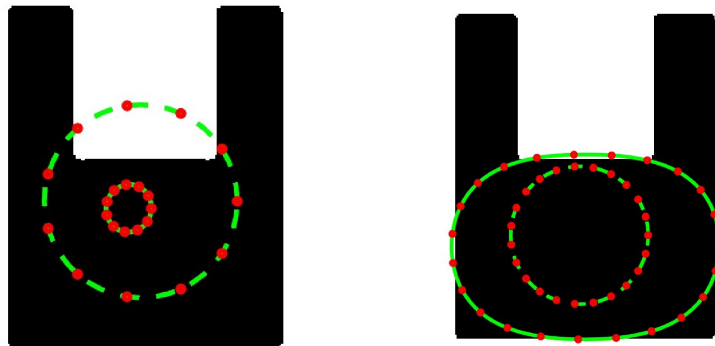


Figure 14: Two examples of bad minima. The initial snake is shown in dashed lines, and the final snake is shown in continuous lines.

needed when the OPI drops and a high value of OPI ensures that the optimization is always progressing in the correct direction.

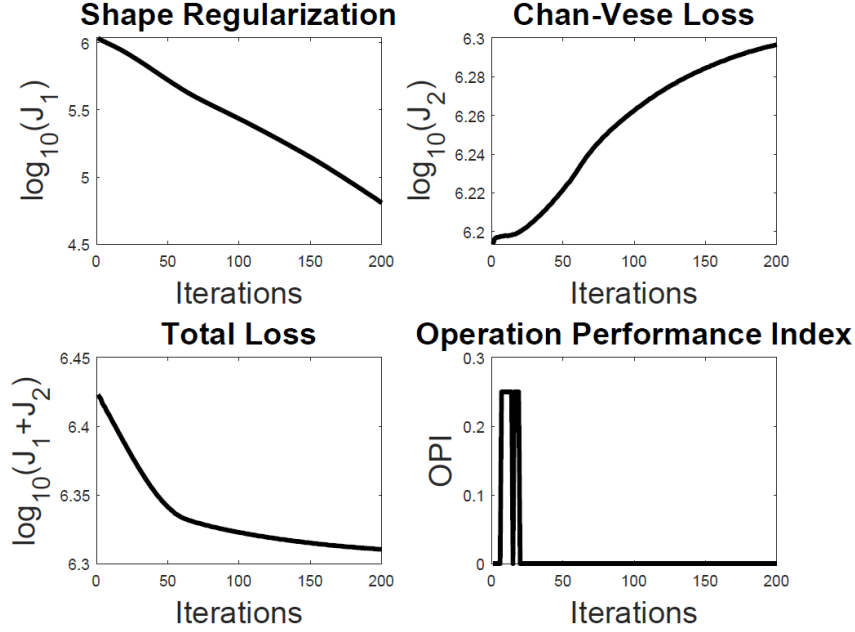


Figure 15: OPI trend (low value throughout) for LHS case of Fig.14. The snake shrinks at all the steps and will ultimately shrink to a point.

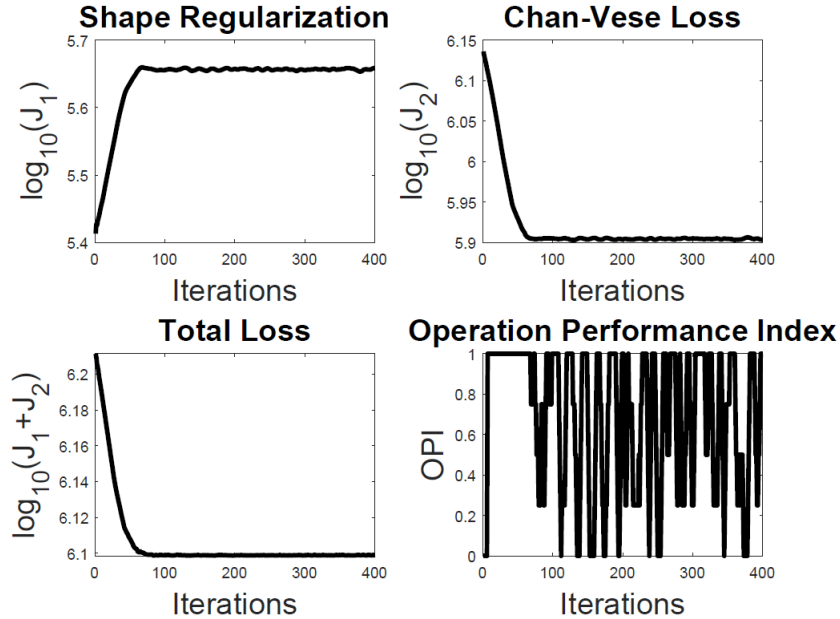


Figure 16: OPI trend (oscillating between 0 and 1) for RHS case of Fig.14. The snake gets stuck in a local minimum after about 100 iterations.

6 Conclusions and Future Work

In this paper, we introduced PICS— an interpretable, physics-informed algorithm for rapid image segmentation in the absence of labeled data. PICS is a novel algorithm that combines the traditional active contour model called snake with the physics-informed neural networks (PINNs). PICS inherits the unique qualities of its parent algorithms (snakes and PINNs), making it intuitive, mesh-free, and respecting the inherent physics of the traditional energy-based loss functions.

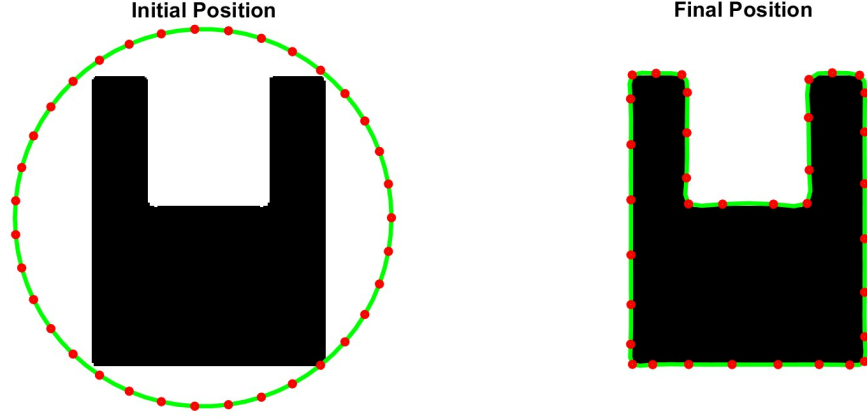


Figure 17: Performance of PICS with adaptive hyperparameters on a u-shaped cavity.

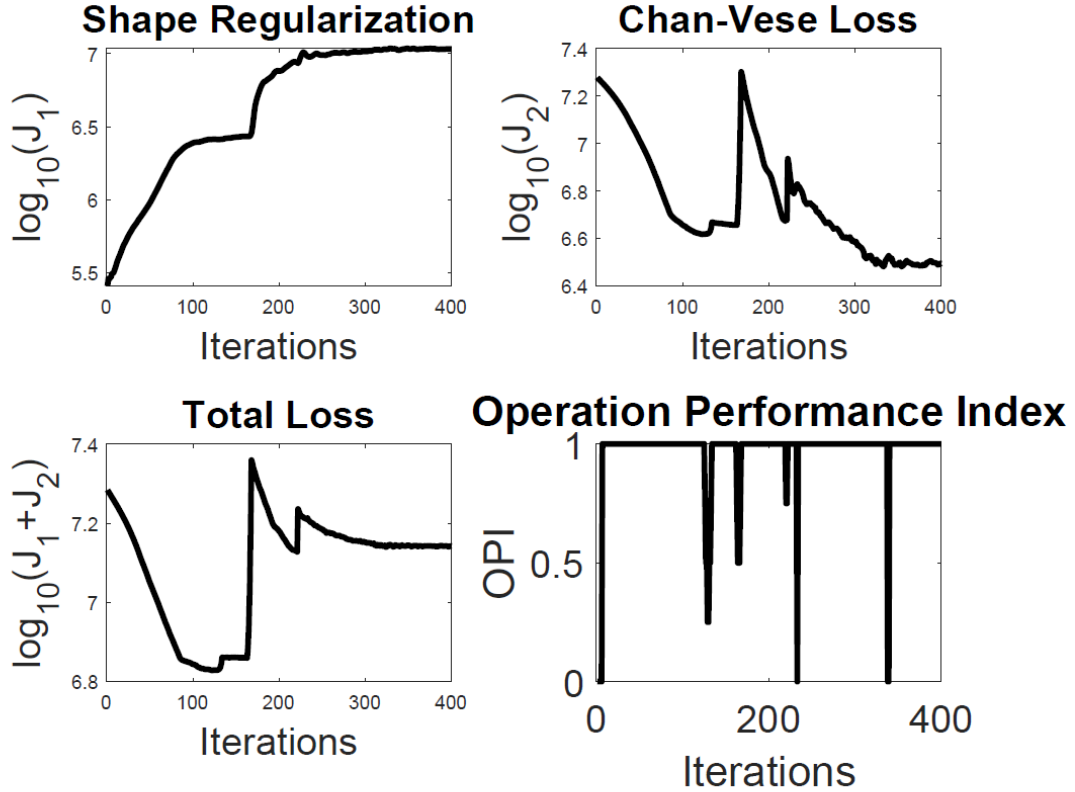


Figure 18: OPI trend of PICS with adaptive hyperparameters for cavity test case.

The use of cubic splines over deep neural network as basis function and the treatment of spline control knots as design variables further increase its interpretability. We demonstrate that PICS is the first work to minimize the Chan-Vese loss in the snake framework and allows for easy integration of medical domain expertise via prior shape-based loss terms. PICS draws a parallel between 3D segmentation and the solution of an unsteady PDE. The results obtained on the ACDC dataset show that it allows PICS to exploit transfer learning and achieve fast segmentation. However, PICS faces challenges in inverse parameter estimation and topology changes during 3D segmentation. To address some of these challenges, we propose a new evaluation metric called Optimization Performance Index (OPI), which allows for adaptive hyperparameter tuning. Overall, PICS demonstrates its effectiveness as an alternative to deep learning-based

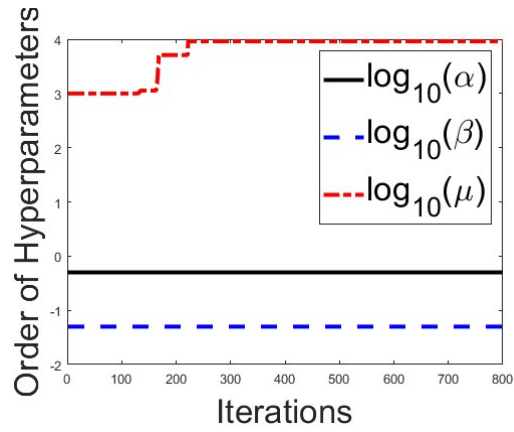


Figure 19: PICS hyperparameters tuning for cavity test case.

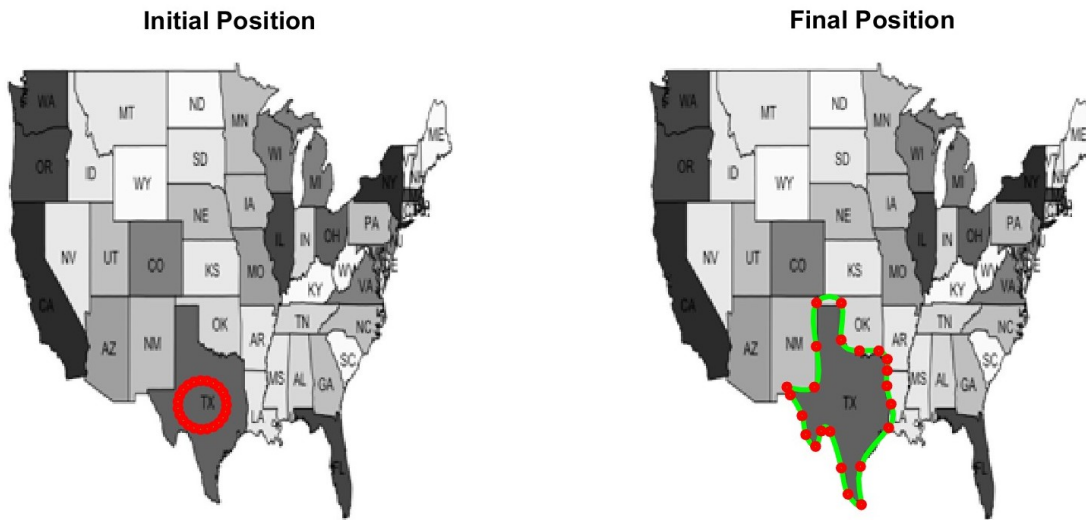


Figure 20: Segmentation of Texas state from the USA map. Left: Initial weights, Right: Optimized weights.

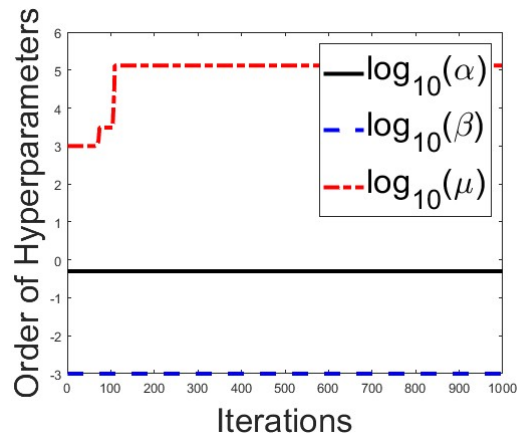


Figure 21: PICS hyperparameters tuning for the USA map case.

segmentation models in the absence of labeled data. It offers a promising solution for medical image segmentation with

its speed, computational efficiency, and human-centered approach, which can significantly reduce the time and cost associated with obtaining labeled training data.

Acknowledgements

This work was supported by the Robert Bosch Centre for Data Science and Artificial Intelligence, Indian Institute of Technology- Madras, Chennai (Project no. SB21221651MERBCX008832).

References

- [1] Chayan Banerjee, Kien Nguyen, Clinton Fookes, and George Karniadakis. Physics-informed computer vision: A review and perspectives, 2023.
- [2] M. Raissi, P. Perdikaris, and G.E. Karniadakis. Physics-informed neural networks: A deep learning framework for solving forward and inverse problems involving nonlinear partial differential equations. *Journal of Computational Physics*, 378:686–707, 2019.
- [3] Maziar Raissi and George Em Karniadakis. Hidden physics models: Machine learning of nonlinear partial differential equations. *Journal of Computational Physics*, 357:125 – 141, 2018.
- [4] Vikas Dwivedi and Balaji Srinivasan. Physics informed extreme learning machine (pielm)—a rapid method for the numerical solution of partial differential equations. *Neurocomputing*, 391:96–118, 2020.
- [5] Dehao Liu and Yan Wang. Multi-Fidelity Physics-Constrained Neural Network and Its Application in Materials Modeling. *Journal of Mechanical Design*, 141(12), 09 2019. 121403.
- [6] Shengze Cai, Zhicheng Wang, Sifan Wang, Paris Perdikaris, and George Em Karniadakis. Physics-Informed Neural Networks for Heat Transfer Problems. *Journal of Heat Transfer*, 143(6), 04 2021. 060801.
- [7] Vikas Dwivedi, Nishant Parashar, and Balaji Srinivasan. Distributed learning machines for solving forward and inverse problems in partial differential equations. *Neurocomputing*, 420:299–316, 2021.
- [8] George Em Karniadakis, Ioannis G. Kevrekidis, Lu Lu, Paris Perdikaris, Sifan Wang, and Liu Yang. Physics-informed machine learning. *Nature Reviews Physics*, 3(6):422–440, Jun 2021.
- [9] Pablo Arratia López, Hernán Mella, Sergio Uribe, Daniel E. Hurtado, and Francisco Sahli Costabal. Warppinn: Cine-mr image registration with physics-informed neural networks. *Medical Image Analysis*, 89:102925, 2023.
- [10] Lucas de Vries, Rudolf L.M. van Herten, Jan W. Hoving, Ivana Išgum, Bart J. Emmer, Charles B.L.M. Majoie, Henk A. Marquering, and Efstratios Gavves. Spatio-temporal physics-informed learning: A novel approach to ct perfusion analysis in acute ischemic stroke. *Medical Image Analysis*, 90:102971, 2023.
- [11] Rudolf L.M. van Herten, Amedeo Chiribiri, Marcel Breeuwer, Mitko Veta, and Cian M. Scannell. Physics-informed neural networks for myocardial perfusion mri quantification. *Medical Image Analysis*, 78:102399, 2022.
- [12] Stefano Buoso, Thomas Joyce, and Sebastian Kozerke. Personalising left-ventricular biophysical models of the heart using parametric physics-informed neural networks. *Medical Image Analysis*, 71:102066, 2021.
- [13] Hendrik Burwinkel, Holger Matz, Stefan Saur, Christoph Hauger, Michael Trost, Nino Hirschall, Oliver Findl, Nassir Navab, and Seyed-Ahmad Ahmadi. Physics-aware learning and domain-specific loss design in ophthalmology. *Medical Image Analysis*, 76:102314, 2022.
- [14] Michael Kass, Andrew Witkin, and Demetri Terzopoulos. Snakes: Active contour models. *International Journal of Computer Vision*, 1(4):321–331, Jan 1988.
- [15] Guillermo Sapiro. *Geometric partial differential equations and image analysis*. Cambridge university press, 2006.
- [16] Chenyang Xu and J.L. Prince. Gradient vector flow: a new external force for snakes. In *Proceedings of IEEE Computer Society Conference on Computer Vision and Pattern Recognition*, pages 66–71, 1997.
- [17] Xianghua Xie and Majid Mirmehdi. Mac: Magnetostatic active contour model. *IEEE Transactions on Pattern Analysis and Machine Intelligence*, 30(4):632–646, 2008.
- [18] Tao Wang, Irene Cheng, and Anup Basu. Fluid vector flow and applications in brain tumor segmentation. *IEEE Transactions on Biomedical Engineering*, 56(3):781–789, 2009.
- [19] Laurent D. Cohen. On active contour models and balloons. *CVGIP: Image Understanding*, 53(2):211–218, 1991.

- [20] Vikas Dwivedi and Balaji Srinivasan. Solution of Biharmonic Equation in Complicated Geometries With Physics Informed Extreme Learning Machine. *Journal of Computing and Information Science in Engineering*, 20(6):061004, 05 2020.
- [21] Vikas Dwivedi and Balaji Srinivasan. A Normal Equation-Based Extreme Learning Machine for Solving Linear Partial Differential Equations. *Journal of Computing and Information Science in Engineering*, 22(1):014502, 07 2021.
- [22] David Bryant Mumford and Jayant Shah. Optimal approximations by piecewise smooth functions and associated variational problems. *Communications on pure and applied mathematics*, 1989.
- [23] Tony F Chan and Luminita A Vese. Active contours without edges. *IEEE Transactions on image processing*, 10(2):266–277, 2001.
- [24] Wenjia Bai, Hideaki Suzuki, Jian Huang, Catherine Francis, Shuo Wang, Giacomo Tarroni, Florian Guitton, Nay Aung, Kenneth Fung, Steffen E Petersen, et al. A population-based phenome-wide association study of cardiac and aortic structure and function. *Nature medicine*, 26(10):1654–1662, 2020.
- [25] Xueyan Mei, Hao-Chih Lee, Kai-yue Diao, Mingqian Huang, Bin Lin, Chenyu Liu, Zongyu Xie, Yixuan Ma, Philip M Robson, Michael Chung, et al. Artificial intelligence-enabled rapid diagnosis of patients with covid-19. *Nature medicine*, 26(8):1224–1228, 2020.
- [26] Philipp Kickingereder, Fabian Isensee, Irada Tursunova, Jens Petersen, Ulf Neuberger, David Bonekamp, Gianluca Brugnara, Marianne Schell, Tobias Kessler, Martha Foltyn, et al. Automated quantitative tumour response assessment of mri in neuro-oncology with artificial neural networks: a multicentre, retrospective study. *The Lancet Oncology*, 20(5):728–740, 2019.
- [27] Li Wang, Dong Nie, Guannan Li, Élodie Puybareau, Jose Dolz, Qian Zhang, Fan Wang, Jing Xia, Zhengwang Wu, Jia-Wei Chen, et al. Benchmark on automatic six-month-old infant brain segmentation algorithms: the iseg-2017 challenge. *IEEE transactions on medical imaging*, 38(9):2219–2230, 2019.
- [28] Vijay Badrinarayanan, Alex Kendall, and Roberto Cipolla. Segnet: A deep convolutional encoder-decoder architecture for image segmentation. *IEEE transactions on pattern analysis and machine intelligence*, 39(12):2481–2495, 2017.
- [29] Jonathan Long, Evan Shelhamer, and Trevor Darrell. Fully convolutional networks for semantic segmentation. In *Proceedings of the IEEE conference on computer vision and pattern recognition*, pages 3431–3440, 2015.
- [30] Olaf Ronneberger, Philipp Fischer, and Thomas Brox. U-net: Convolutional networks for biomedical image segmentation. In *Medical Image Computing and Computer-Assisted Intervention—MICCAI 2015: 18th International Conference, Munich, Germany, October 5-9, 2015, Proceedings, Part III 18*, pages 234–241. Springer, 2015.
- [31] Geert Litjens, Thijs Kooi, Babak Ehteshami Bejnordi, Arnaud Arindra Adiyoso Setio, Francesco Ciompi, Mohsen Ghafoorian, Jeroen Awm Van Der Laak, Bram Van Ginneken, and Clara I Sánchez. A survey on deep learning in medical image analysis. *Medical image analysis*, 42:60–88, 2017.
- [32] Dinggang Shen, Guorong Wu, and Heung-II Suk. Deep learning in medical image analysis. *Annual review of biomedical engineering*, 19:221–248, 2017.
- [33] Mohammad Hesam Hesamian, Wenjing Jia, Xiangjian He, and Paul Kennedy. Deep learning techniques for medical image segmentation: achievements and challenges. *Journal of digital imaging*, 32:582–596, 2019.
- [34] Xiaomeng Li, Hao Chen, Xiaojuan Qi, Qi Dou, Chi-Wing Fu, and Pheng-Ann Heng. H-denseunet: hybrid densely connected unet for liver and tumor segmentation from ct volumes. *IEEE transactions on medical imaging*, 37(12):2663–2674, 2018.
- [35] Jose Dolz, Karthik Gopinath, Jing Yuan, Herve Lombaert, Christian Desrosiers, and Ismail Ben Ayed. Hyperdense-net: a hyper-densely connected cnn for multi-modal image segmentation. *IEEE transactions on medical imaging*, 38(5):1116–1126, 2018.
- [36] Matthias G Haberl, Christopher Churas, Lucas Tindall, Daniela Boassa, Sébastien Phan, Eric A Bushong, Matthew Madany, Raffi Akay, Thomas J Deerinck, Steven T Peltier, et al. Cdeep3m—plug-and-play cloud-based deep learning for image segmentation. *Nature methods*, 15(9):677–680, 2018.
- [37] Saba Rahimi, Ozan Oktay, Javier Alvarez-Valle, and Sujeeth Bharadwaj. Addressing the exorbitant cost of labeling medical images with active learning. In *International Conference on Machine Learning in Medical Imaging and Analysis*, page 1, 2021.
- [38] Yann LeCun, Yoshua Bengio, and Geoffrey Hinton. Deep learning. *nature*, 521(7553):436–444, 2015.
- [39] Sarah Webb et al. Deep learning for biology. *Nature*, 554(7693):555–557, 2018.

- [40] Zachary C. Lipton. The doctor just won't accept that!, 2017.
- [41] WP Segars, Jason Bond, Jack Frush, Sylvia Hon, Chris Eckersley, Cameron H Williams, Jianqiao Feng, Daniel J Tward, JT Ratnanather, MI Miller, et al. Population of anatomically variable 4d xcat adult phantoms for imaging research and optimization. *Medical physics*, 40(4):043701, 2013.
- [42] Ozan Oktay, Jay Nanavati, Anton Schwaighofer, David Carter, Melissa Bristow, Ryutaro Tanno, Rajesh Jena, Gill Barnett, David Noble, Yvonne Rimmer, et al. Evaluation of deep learning to augment image-guided radiotherapy for head and neck and prostate cancers. *JAMA network open*, 3(11):e2027426–e2027426, 2020.
- [43] Juan Manuel Durán and Karin Rolanda Jongsma. Who is afraid of black box algorithms? on the epistemological and ethical basis of trust in medical ai. *Journal of Medical Ethics*, 47(5):329–335, 2021.
- [44] Atnes Baydin, Barak A. Pearlmutter, Alexey Andreyevich Radul, and Jeffrey Mark Siskind. Automatic differentiation in machine learning: A survey. *J. Mach. Learn. Res.*, 18(1):5595–5637, January 2017.
- [45] Moshe Shimrat. Algorithm 112: position of point relative to polygon. *Communications of the ACM*, 5(8):434, 1962.
- [46] Diederik P. Kingma and Jimmy Ba. Adam: A method for stochastic optimization, 2014.
- [47] Xue Shi and Chunming Li. Convexity preserving level set for left ventricle segmentation. *Magnetic Resonance Imaging*, 78:109–118, 2021.
- [48] Olivier Bernard, Alain Lalande, Clement Zotti, Frederick Cervenansky, Xin Yang, Pheng-Ann Heng, Irem Cetin, Karim Lekadir, Oscar Camara, Miguel Angel Gonzalez Ballester, et al. Deep learning techniques for automatic mri cardiac multi-structures segmentation and diagnosis: is the problem solved? *IEEE transactions on medical imaging*, 37(11):2514–2525, 2018.
- [49] Bastian Zapf, Johannes Haubner, Miroslav Kuchta, Geir Ringstad, Per Kristian Eide, and Kent-Andre Mardal. Investigating molecular transport in the human brain from mri with physics-informed neural networks. *Scientific Reports*, 12(1):15475, 2022.